

# Reference-Free Multi-Modality Volume Registration of X-Ray Microscopy and Light-Sheet Fluorescence Microscopy

Siyuan Mei<sup>1</sup>, Fuxin Fan<sup>1</sup>, Mareike Thies<sup>1</sup>, Mingxuan Gu<sup>1</sup>, Fabian Wagner<sup>1</sup>, Oliver Aust<sup>2</sup>, Ina Erceg<sup>3</sup>, Zeynab Mirzaei<sup>4</sup>, Georgiana Neag<sup>2</sup>, Yipeng Sun<sup>1</sup>, Yixing Huang<sup>2</sup>, and Andreas Maier<sup>1</sup>

<sup>1</sup> Friedrich-Alexander University Erlangen-Nürnberg, Erlangen, Germany

<sup>2</sup> University Hospital Erlangen, Erlangen, Germany

<sup>3</sup> Fraunhofer Institute for Ceramic Technologies and Systems IKTS, Forchheim, Germany

<sup>4</sup> Institut für Nanotechnologie und korrelative Mikroskopie – INAM GmbH, Forchheim, Germany  
siyuan.mei@fau.de

**Abstract.** Recently, X-ray microscopy (XRM) and light-sheet fluorescence microscopy (LSFM) have emerged as two pivotal imaging tools in preclinical research on bone remodeling diseases, offering micrometer-level resolution. Integrating these complementary modalities provides a holistic view of bone microstructures, facilitating function-oriented volume analysis across different disease cycles. However, registering such independently acquired large-scale volumes is extremely challenging under real and reference-free scenarios. This paper presents a fast two-stage pipeline for volume registration of XRM and LSFM. The first stage extracts the surface features and employs two successive point cloud-based methods for coarse alignment. The second stage fine-tunes the initial alignment using a modified cross-correlation method, ensuring precise volumetric registration. Moreover, we propose residual similarity as a novel metric to assess the alignment of two complementary modalities. The results imply robust gradual improvement across the stages. In the end, all correlating microstructures, particularly lacunae in XRM and bone cells in LSFM, are precisely matched, enabling new insights into bone diseases like osteoporosis which are a substantial burden in aging societies.

**Keywords:** 3D rigid registration · Multi-modality · High-resolution volume · Surface-to-volumetric.

## 1 Introduction

Osteoporosis (OP) has become a major health concern in aging societies, which markedly increases the risk of fragility fractures and related conditions. In Europe alone, over 27 million individuals suffered from OP, with this number expected to rise sharply owing to demographic aging trends [8]. Traditional medical

understanding of OP primarily revolves around the reduced bone mass resulting from imbalanced bone remodeling [17], which can be recognized by conventional imaging modalities, such as computed tomography (CT), magnetic resonance imaging (MRI), and ultrasonography (US) [12]. However, their insufficient resolution prevents deepening into the mechanisms of micro-architectural deterioration at the scale of the osteocyte system. To revolutionize today’s knowledge, recent research has pioneered the creation of volumetric bone models at the micrometer level using newly available imaging tools, specifically, X-ray microscopy (XRM) [11] and light-sheet fluorescence microscopy (LSFM) [23]. These cutting-edge modalities provide complementary 3D views, with XRM revealing detailed bone morphology and LSFM highlighting cellular and vascular structures inside the bones (see instances in the leftmost part of Fig. 1 or refer to full-sized images in Supplementary Material). Initial attempts combining these modalities supported by expert observation have unveiled the significance of small transcortical vessels [6]. Nonetheless, this manual approach is not only laborious but also falls short for finer structures, such as lacunae and stained bone cells, due to their considerably smaller size (diameter under  $5\ \mu\text{m}$ ). To advance this research and fully leverage information in these scans, developing an automated algorithm for precise registration of XRM and LSFM volumes comes on priority.

The most frequently used methods estimating rigid transformation parameters (3D rotation and translation) between two multi-modality 3D medical images rely on extracting common features from both modalities, such as surface contours and anatomical landmarks [20, 25]. As an easily available feature without the need for annotations, surface-based approaches [1, 7, 10] perform reliably by finding point-to-point correspondence using matching techniques like iterative closest points (ICP) [2, 27]. However, surface features restrict themselves only to a subset of the available volumetric information. In contrast, mutual information-based methods [16, 22] take full image contents into account and iteratively optimize transformation parameters to reach a maximum similarity measure. Despite their popularity, these methods are infeasible for large-sized volumes, because each iteration step requires an intermediate transformation interpolating the entire volume which is extremely time-consuming. Moreover, recent unsupervised learning-based methods [13, 26] register image data by utilizing deep convolutional layers to extract 3D features and regressing the transformation parameters using spatial transformer layers [9]. Unfortunately, for clinical applications involving biological samples, often only few volume pairs are available. Further, training a deep neural network demands substantial memory resources when down-scaling is undesirable.

To overcome these challenges, we propose an innovative two-stage registration pipeline for XRM and LSFM volumes, as illustrated in Fig. 1. Given a volume pair as input, the first stage starts from the surface extraction and then performs global-to-local point cloud registration, offering a coarse alignment. Crucially, this initial alignment is fine-tuned in the second stage by efficiently searching for the remaining transformation in the Fourier domain based on a modified cross-correlation method. The main contributions are summarized as follows:

- This is **the first** work that successfully performs automatic registration between high-resolution XRM and LSFM volumes while attaining micrometer-scale accuracy.
- The combination of point cloud-based and cross-correlation methods considers both surface features and full image contents, achieving coarse to fine registration within two stages.
- An effective evaluation metric, i.e., residual similarity, is proposed to quantitatively assess the alignment of two complementary modalities under reference-free scenarios. All registration and evaluation codes will be released.

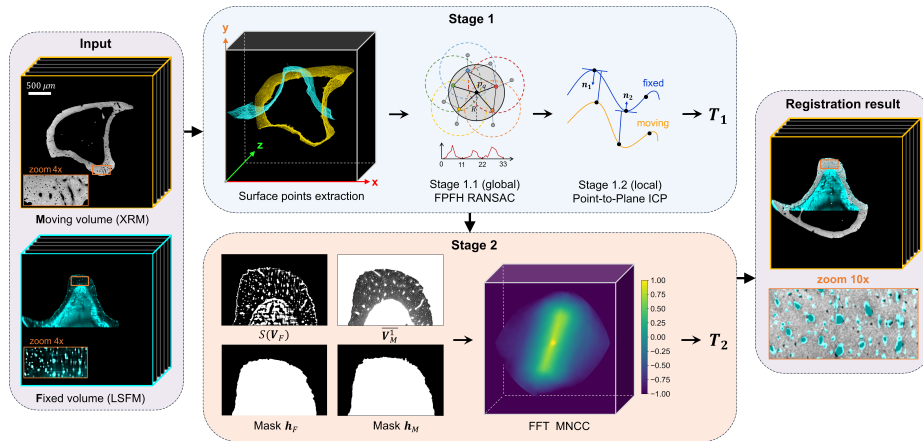


Fig. 1: Two-stage volume registration pipeline. (LSFM volume is colored in cyan to distinguish it from XRM volume)

## 2 Materials and Methods

In the preclinical context, carefully prepared ex-vivo mouse tibia samples across varying ages and health conditions are imaged to investigate the bone remodeling process. The illustration of data acquisition procedures of XRM and LSFM with respective 3D-rendered volumes is detailed in Supplementary Material A.

### 2.1 Data Description and Preprocessing

XRM, known for its high contrast capability, presents bone structures at higher intensity against soft tissues' markedly lower intensity. This modality allows for the 3D reconstruction of bones with micrometer optical resolution, resolving the hard microstructures affected during the bone remodeling process, such as blood vessel canals and lacunae. Conversely, LSFM is an optical imaging method that

highlights the functional soft tissues for bone remodelings, such as vessels, bone cells, and bone marrow. Before imaging, soft tissues are labeled with specific fluorescent stains, and bones are rendered transparent to ensure optimal visualization [21]. LSFM images capture the fluorescing soft tissues with high intensity, thereby offering a complementary view to those obtained by XRM.

Given the use of independent imaging devices, the acquired raw data differ in volume dimensions and voxel sizes. Specifically, XRM reconstruction volumes are characterized by a volume shape (height  $\times$  width  $\times$  slices) of  $1997 \times 2038 \times 2014$  with a voxel size of  $1.42 \times 1.42 \times 1.42 \mu\text{m}$ , while LSFM volumes feature a volume shape of  $2048 \times 2048 \times 504$  with a voxel size of  $1.51 \times 1.51 \times 4.00 \mu\text{m}$ . To standardize the data for registration, we undertake several preprocessing steps for each volume pair: Firstly, the LSFM volume is resliced and rescaled to match the XRM scan’s coordinate system and resolution; Secondly, the distal bone segments comprising 800 slices are selected to focus on medically most relevant regions; Finally, both volumes are zero-padded to achieve uniform dimensions of  $2048 \times 2048 \times 800$ . An example of central slices from the processed volume pair is depicted in the leftmost part of Fig. 1, with the microstructures of interest magnified in the subregions. Notably, the lower portion of the bone cross-section in the LSFM volume has not been acquired due to significant scattering noise. In the following registration process, we define XRM as the moving volume ( $\mathbf{V}_M$ ) and LSFM as the fixed volume ( $\mathbf{V}_F$ ).

## 2.2 First Stage: Surface Point Cloud Registration

The first stage of the registration pipeline starts with extracting surface point clouds from two volumes. This is readily achieved by executing thresholding binarization ( $\mathbf{V}_M > 5$  and  $\mathbf{V}_F > 0$ ), followed by a series of binary morphological operations (namely, binary closing, hole filling, and outlining) for each 2D slice. As illustrated in the upper middle part of Fig. 1, the moving point cloud  $\mathbf{P}_M \in \mathbb{Z}^{3 \times N_M}$  is rendered in yellow, whereas the fixed point cloud  $\mathbf{P}_F \in \mathbb{Z}^{3 \times N_F}$  is rendered in cyan. After obtaining these two surface point clouds, their central points are first aligned to reduce the initial gap for registration.

**Stage 1.1: FPFH RANSAC** Subsequently, both point clouds are mapped into a 33-dimensional fast point feature histogram (FPFH) feature space [18], which captures the local geometric characteristics of each point. The core of this stage involves the application of the RANSAC algorithm [5] to fit a rigid transformation model between two point clouds, following these steps:

- (i) Randomly select three points from  $\mathbf{P}_M$  and detect their corresponding points in  $\mathbf{P}_F$  by querying the nearest neighbors in the FPFH feature space.
- (ii) For these matched point pairs, compute a hypothesized transformation matrix  $\mathbf{T} \in \mathbb{R}^{4 \times 4}$  based on least-squares estimation [24].
- (iii) Apply  $\mathbf{T}$  to  $\mathbf{P}_M$  and determine the inlier count, where inliers are defined as matched point pairs with distances below a specified threshold.

- (iv) Iterate the above steps until reaching either the predefined iteration limit (100000) or statistical confidence (0.999) of consensus among inliers.

This procedure results in the initial transformation matrix  $\mathbf{T}_{1,1}$ , fitted with the highest number of inliers.

**Stage 1.2: Point-to-Plane ICP** Due to random sampling, the FPFH RANSAC algorithm only offers a suboptimal solution for global registration. Therefore, a local refinement is required to pursue a tighter surface alignment. We integrate the point-to-plane ICP [4] following a widely used workflow in point cloud registration [19, 28]. This method improves the initial transformation  $\mathbf{T}_{1,1}$  through the following iteration steps:

- (i) Apply the current transformation  $\mathbf{T}$  to  $\mathbf{P}_M$ , obtaining  $\mathbf{P}'_M$ .
- (ii) Identify all closest point pairs  $\mathcal{P}\{(\mathbf{p}'_M^{(i)}, \mathbf{p}_F^{(i)})\}$  between  $\mathbf{P}'_M$  and  $\mathbf{P}_F$ .
- (iii) Update  $\mathbf{T}$  by minimizing the following objective function with the Gauss-Newton optimizer

$$\mathcal{L}(\mathbf{T}) = \sum_{(\mathbf{p}'_M^{(i)}, \mathbf{p}_F^{(i)}) \in \mathcal{P}} [\mathbf{n}^{(i)} \cdot (\mathbf{p}_F^{(i)} - \mathbf{T}\mathbf{p}'_M^{(i)})]^2, \quad (1)$$

where  $\mathbf{n}^{(i)}$  is the surface normal vector of point  $\mathbf{p}_F^{(i)}$ .

- (iv) Repeat the above steps until the relative increment of the inlier number converges or a maximum iteration count (2000) is reached.

At the end of this process, the refined transformation  $\mathbf{T}_{1,2}$  that accurately aligns the two point clouds is derived. The output of the first stage is updated as  $\mathbf{T}_1 = \mathbf{T}_{1,2}$ , and the transformed XRM volume is  $\mathbf{V}_M^1 = a(\mathbf{V}_M, \mathbf{T}_1)$ , where  $a(\cdot)$  represents the affine transformation with bicubic interpolation.

### 2.3 Second Stage: Volumetric Registration

Following the surface registration, a fine-tuning stage is essential to address the remaining misalignments of microstructures within the bone. Re-observing the image contents in Fig. 1, vessel canals and lacunae appear as tiny holes with close-to-zero intensity in XRM volumes, contrast sharply with the bright, high-intensity representations of stained vessels and cells in LSFM volumes. These opposite intensity features can be matched by inverting the voxel intensity of XRM volume, yielding  $\overline{\mathbf{V}_M^1}$ . To eliminate the influence of the background outside the bone, binary bone masks  $\mathbf{h}_F$  and  $\mathbf{h}_M$  are generated for LSFM volume and the transformed XRM volume respectively using thresholding at zero followed by hole-filling operations. In addition, we apply a sharpening step with the unsharp mask algorithm [14] for LSFM to reduce the scattering noise and enhance feature clarity, producing  $S(\mathbf{V}_F)$ . Illustrative examples of four cropped slices from  $S(\mathbf{V}_F)$  with mask  $\mathbf{h}_F$  and  $\overline{\mathbf{V}_M^1}$  with mask  $\mathbf{h}_M$  are shown in the lower middle part of Fig. 1. For brevity, we redefine  $S(\mathbf{V}_F) \odot \mathbf{h}_F$  as  $\mathbf{V}_1$  and  $\overline{\mathbf{V}_M^1} \odot \mathbf{h}_M$  as  $\mathbf{V}_2$ .

Now, the high-intensity voxels in both  $\mathbf{V}_1$  and  $\mathbf{V}_2$  present the same semantic in bones. A perfect registration is found as an optimal transformation  $\mathbf{T}_2^*$  which maximizes the sum of the product of  $\mathbf{V}_1$  and  $a(\mathbf{V}_2, \mathbf{T}_2)$ . Since the large displacement and rotation have been compensated during the surface registration phase, the remaining transformation can be approximated as a tight 3D translation  $[\Delta x, \Delta y, \Delta z]$ . Thus, an exhaustive search of  $\mathbf{T}_2$  can be conducted using masked normalized cross-correlation (MNCC), formulated as

$$MNCC(\mathbf{T}_2) = \frac{\sum [(\mathbf{V}_1 - \mu_1)(a(\mathbf{V}_2, \mathbf{T}_2) - \mu_2)]}{\sqrt{\sum (\mathbf{V}_1 - \mu_1)^2} \sqrt{\sum (a(\mathbf{V}_2, \mathbf{T}_2) - \mu_2)^2}}, \quad (2)$$

where  $\mu_1$  and  $\mu_2$  represent the mean value of  $\mathbf{V}_1$  and  $a(\mathbf{V}_2, \mathbf{T}_2)$  in the overlapping region of  $\mathbf{h}_F$  and  $a(\mathbf{h}_M, \mathbf{T}_2)$ .

Like the cross-correlation in the spatial domain has its dual in the Fourier domain [3], MNCC also has a corresponding Fourier version [15], enabling efficient computation across all potential  $\mathbf{T}_2$  simultaneously using the fast Fourier transform (FFT). This approach circumvents the need for direct transformations in the spatial domain, significantly speeding up the registration process. The outcome of the FFT MNCC operation is a comprehensive search space with the same size as the original volume, as illustrated in the lower middle section of Fig. 1. Each coordinate represents a relative translation ( $[0, 0, 0]$  at the center), and the intensity corresponds to the MNCC score within the range of  $[-1, 1]$ . The optimal transformation  $\mathbf{T}_2^*$  is identified as the offset from the center to the location with the peak correlation score. Consequently, the overall transformation, combining both stages, is given as  $\mathbf{T}_{overall} = \mathbf{T}_2^* \mathbf{T}_1$ .

#### 2.4 Evaluation Strategy: Residual Similarity

Although a higher MNCC score indicates better alignment, it lacks a reference standard, such as a ground truth for optimal alignment. Alternatively, evaluation via mutual information, which gauges statistical dependence between voxel intensities of two different image modalities, also encounters difficulties due to the significant deviation in intensity distributions. Given the completely complementary nature between XRM and LSFM modalities, we propose *residual similarity* (RS) for the quantitative evaluation of registration accuracy, which is defined as

$$RS(\mathbf{x}, \mathbf{y}, \mathbf{h}_x, \mathbf{h}_y) = sim(\mathbf{y} - clip(\mathbf{y} - \mathbf{x})) + \lambda \times \left(1 - \frac{2 \sum \mathbf{h}_x \odot \mathbf{h}_y}{\sum \mathbf{h}_x + \sum \mathbf{h}_y}\right), \quad (3)$$

where the similarity function  $sim(\cdot)$  can be mean absolute error (MAE) or root mean square error (RMSE),  $\mathbf{x}$  and  $\mathbf{y}$  are specified as the sharpened LSFM volume and the transformed XRM volume with  $\mathbf{h}_x$  and  $\mathbf{h}_y$  being their respective bone masks, and  $\lambda = 100$  is a heuristic weighting factor. In the first term, the distance between the label  $\mathbf{y}$  and the residual volume  $(\mathbf{y} - \mathbf{x})$  with the clipped data range of  $[0, 255]$  is measured, where the residual volume reflects the extent to which  $\mathbf{y}$  is destroyed by  $\mathbf{x}$ . Further, the second term is applied to punish the low value of the first term resulting from less overlap. Therefore, the lower RS values correspond to superior registration performance.

### 3 Experiments

In total, seven ex-vivo mouse tibial samples were independently scanned by XRM and LSFM to generate a set of corresponding volume pairs (see details of devices and parameters in Supplementary Material B). The preparation of all samples received approval from the local animal ethics committees of the Regierung von Mittelfranken (TS-12/2015) and adhered to the guidelines of the Federation of European Laboratory Animal Science Associations.

Codes of the entire workflow were implemented in Python and C++. Note that the whole registration pipeline can be efficiently executed on a modest hardware setup (we just use an Intel i5-13500 CPU with 64 GB RAM), underscoring the low-resource requirement of the proposed method.

### 4 Results and Discussion

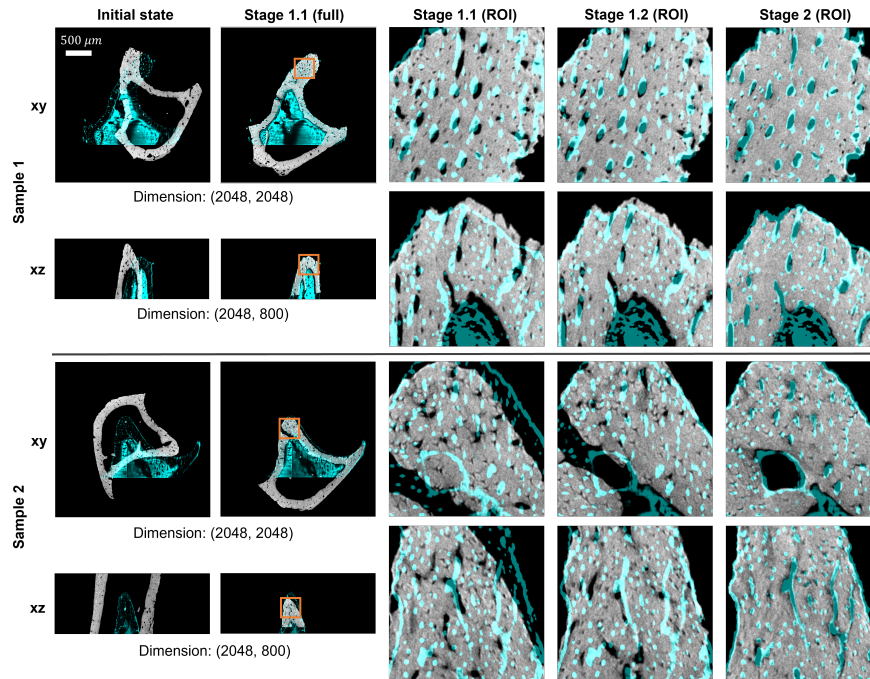


Fig. 2: Visualization of fused images under different stages. Every two rows display orthogonal central slices from the  $xy$ - and  $xz$ -plane of one testing sample. The first two columns show the entire views at the initial state and stage 1.1, respectively, with specified dimensions. Subsequent columns highlight eightfold magnified regions of interest (ROIs) from the  $256 \times 256$  orange boxes through successive registration stages.

We demonstrate the gradual improvement in registration accuracy across the stages. Two samples with distinct bone shapes are shown in Fig. 2. As shown in the first two columns, the entire volumes are coarsely 3D aligned at stage 1.1 even with the bad initial state. This coarseness, which can be observed in the misaligned microstructures in the third column, is gradually refined through the subsequent registration stages. The best results are achieved at stage 2, where all microstructures are precisely matched. For quantitative evaluation, we select subvolumes with the size of  $500 \times 500 \times 400$  which are the uppermost bone segments with the optimal image quality and dense microstructures. Evaluation metrics include the overlap ratio of the binary bone masks, residual MAE, and residual RMSE (as described in Section 2.4). Table 1 summarizes the averaged results of all seven volume pairs. Corresponding to the qualitative results, stage 1.1 greatly increases the overlap ratio and lowers the residual MAE and residual RMSE compared to the initial state, then these values are improved in stage 1.2 and reach the optimum in stage 2.

Table 1: Quantitative results on microstructure-dense regions.

Stage	Initial state	Stage 1.1	Stage 1.2	Stage 2
Overlap ratio ( $\uparrow$ )	$0.43 \pm 0.23$	$0.95 \pm 0.04$	$0.98 \pm 0.01$	$0.98 \pm 0.01$
Residual MAE ( $\downarrow$ )	$60.04 \pm 22.26$	$11.60 \pm 3.73$	$8.37 \pm 1.35$	$7.97 \pm 1.19$
Residual RMSE ( $\downarrow$ )	$74.63 \pm 20.47$	$32.96 \pm 4.69$	$28.67 \pm 3.51$	$25.12 \pm 2.63$
Time cost (s)	/	3.50	15.59	45.65

The computation times of each stage in the last row of Table 1 demonstrate the method’s efficiency for processing large volume datasets. However, stage 2 is still constrained to estimating translations, omitting slight rotational adjustments. This oversight might cause some false matches between tiny lacunae and osteocytes, potentially impacting the accuracy of clinical analyses related to bone remodeling. Future work will aim to extend stage 2 to six degrees of freedom or to develop an end-to-end framework.

## 5 Conclusion

We present an automatic two-stage registration pipeline for high-resolution XRM and LSFM volumes, which achieves 98% overlap ratio of objective areas and observable precisely aligned microstructures. With the successful fusion of two image modalities, it is for the first time possible to conduct large-scale studies quantifying the proportion of lacunae that contain osteocyte cells as a potential new biomarker for bone remodeling diseases.

**Acknowledgement.** This work was supported by the European Research Council (ERC Grant No. 810316). Data was collected at the university hospital Erlangen, INAM, and IKTS.

## References

1. Almhdie, A., Léger, C., Deriche, M., Lédée, R.: 3d registration using a new implementation of the icp algorithm based on a comprehensive lookup matrix: Application to medical imaging. *Pattern Recognition Letters* **28**(12), 1523–1533 (2007)
2. Besl, P.J., McKay, N.D.: Method for registration of 3-d shapes. In: *Sensor fusion IV: control paradigms and data structures*. vol. 1611, pp. 586–606. Spie (1992)
3. Bracewell, R., Kahn, P.B.: The fourier transform and its applications. *American Journal of Physics* **34**(8), 712–712 (1966)
4. Chen, Y., Medioni, G.: Object modelling by registration of multiple range images. *Image and vision computing* **10**(3), 145–155 (1992)
5. Fischler, M.A., Bolles, R.C.: Random sample consensus: a paradigm for model fitting with applications to image analysis and automated cartography. *Communications of the ACM* **24**(6), 381–395 (1981)
6. Grüneboom, A., Hawwari, I., Weidner, D., Culemann, S., Müller, S., Henneberg, S., Brenzel, A., Merz, S., Bornemann, L., Zec, K., et al.: A network of trans-cortical capillaries as mainstay for blood circulation in long bones. *Nature metabolism* **1**(2), 236–250 (2019)
7. Harada, K., Kim, H., Tan, J.K., Ishikawa, S., Yamamoto, A.: Optimal registration method based on icp algorithm from head ct and mr image sets. In: *2008 International Conference on Control, Automation and Systems*. pp. 1268–1271. IEEE (2008)
8. Hernlund, E., Svedbom, A., Ivergård, M., Compston, J., Cooper, C., Stenmark, J., McCloskey, E.V., Jönsson, B., Kanis, J.A.: Osteoporosis in the european union: medical management, epidemiology and economic burden: a report prepared in collaboration with the international osteoporosis foundation (iof) and the european federation of pharmaceutical industry associations (efpia). *Archives of osteoporosis* **8**, 1–115 (2013)
9. Jaderberg, M., Simonyan, K., Zisserman, A., et al.: Spatial transformer networks. *Advances in neural information processing systems* **28** (2015)
10. Kagadis, G.C., Delibasis, K.K., Matsopoulos, G.K., Mouravliansky, N.A., Asvestas, P.A., Nikiforidis, G.C.: A comparative study of surface-and volume-based techniques for the automatic registration between ct and spect brain images. *Medical Physics* **29**(2), 201–213 (2002)
11. Langer, M., Peyrin, F.: 3d x-ray ultra-microscopy of bone tissue. *Osteoporosis International* **27**, 441–455 (2016)
12. Link, T.M.: Osteoporosis imaging: state of the art and advanced imaging. *Radiology* **263**(1), 3–17 (2012)
13. Mok, T.C., Chung, A.: Affine medical image registration with coarse-to-fine vision transformer. In: *Proceedings of the IEEE/CVF Conference on Computer Vision and Pattern Recognition*. pp. 20835–20844 (2022)
14. Morishita, K., Yamagata, S., Okabe, T., Yokoyama, T., Hamatani, K.: Unsharp masking for image enhancement (Dec 27 1988), uS Patent 4,794,531
15. Padfield, D.: Masked object registration in the fourier domain. *IEEE Transactions on image processing* **21**(5), 2706–2718 (2011)
16. Pluim, J.P., Maintz, J.A., Viergever, M.A.: Mutual-information-based registration of medical images: a survey. *IEEE transactions on medical imaging* **22**(8), 986–1004 (2003)
17. Raggatt, L.J., Partridge, N.C.: Cellular and molecular mechanisms of bone remodeling. *Journal of biological chemistry* **285**(33), 25103–25108 (2010)

18. Rusu, R.B., Blodow, N., Beetz, M.: Fast point feature histograms (FPFH) for 3D registration. In: 2009 IEEE international conference on robotics and automation. pp. 3212–3217. IEEE (2009)
19. Rusu, R.B., Cousins, S.: 3d is here: Point cloud library (pcl). In: 2011 IEEE international conference on robotics and automation. pp. 1–4. IEEE (2011)
20. Saiti, E., Theoharis, T.: An application independent review of multimodal 3d registration methods. *Computers & Graphics* **91**, 153–178 (2020)
21. Santi, P.A.: Light sheet fluorescence microscopy: a review. *Journal of Histochemistry & Cytochemistry* **59**(2), 129–138 (2011)
22. Studholme, C., Hill, D.L., Hawkes, D.J.: An overlap invariant entropy measure of 3d medical image alignment. *Pattern recognition* **32**(1), 71–86 (1999)
23. Thai, J., Fuller-Jackson, J.P., Ivanusic, J.J.: Using tissue clearing and light sheet fluorescence microscopy for the three-dimensional analysis of sensory and sympathetic nerve endings that innervate bone and dental tissue of mice. *Journal of Comparative Neurology* **532**(1), e25582 (2024)
24. Umeyama, S.: Least-squares estimation of transformation parameters between two point patterns. *IEEE Transactions on Pattern Analysis & Machine Intelligence* **13**(04), 376–380 (1991)
25. Viergever, M.A., Maintz, J.A., Klein, S., Murphy, K., Staring, M., Pluim, J.P.: A survey of medical image registration—under review (2016)
26. Wang, A.Q., Evan, M.Y., Dalca, A.V., Sabuncu, M.R.: A robust and interpretable deep learning framework for multi-modal registration via keypoints. *Medical Image Analysis* **90**, 102962 (2023)
27. Yang, J., Li, H., Campbell, D., Jia, Y.: Go-icp: A globally optimal solution to 3d icp point-set registration. *IEEE transactions on pattern analysis and machine intelligence* **38**(11), 2241–2254 (2015)
28. Zhou, Q.Y., Park, J., Koltun, V.: Open3d: A modern library for 3d data processing. arXiv preprint arXiv:1801.09847 (2018)